On the geometry of fracture and frustration

Koning, V.

Cover Page

The handle http://hdl.handle.net/1887/29873 holds various files of this Leiden University dissertation.

Author: Koning, Vinzenz
Title: On the geometry of fracture and frustration
Issue Date: 2014-11-26

THICK SHELLS

3.1 INTRODUCTION

Many systems in condensed matter physics and elasticity can be treated as two-dimensional, though only very few, like graphene [74] and colloidal crystals at liquid-liquid interfaces [21, 4, 34], are truly *mono*layers. The theory of plates and membranes [44], superfluid [102] and liquid crystal films [6] can all be neatly described by a reduction of the number of spatial dimensions from three to two by assuming that the thickness is small compared to the other two dimensions and approximately constant. This reduction of dimensions usually simplifies the analysis significantly, because the number of variables to solve for is reduced and in addition one can employ well developed mathematical machinery such as complex analysis that is well suited to tackle two-dimensional problems. For instance, the use of conformal mappings has been applied successfully in superfluid films [102]. Another example of the use of a conformal mapping was in the study of the tetravalent defect configuration in a two-dimensional nematic on a spherical surface [57]. From the previous chapter (chapter 2) we learned that a finite shell thickness allows for shells with different valency. Experiments on nematic double emulsion droplets also show that the thickness inhomogeneity of the shell plays a crucial role [56]. Since the density difference between the inner drop and the liquid crystal, buoyancy displaces the inner drop out of the centre of the larger drop along the gravitational direction, as shown schematically in Fig. 10. This leads to a rich variety of defect structures, as shown in Fig. 21. One of the striking manifestations of the inhomogeneity are very abrupt confinement and deconfinement transitions in shells with two pairs of surface defects, called boojums[1]. When the shell is rather thick and homogeneous, the two pairs

---

1 At this point it is interesting to note that in the solid analogue of the liquid crystal shell, thickness inhomogeneity is also important. It affects the buckling and folding of these solid capsules [16].
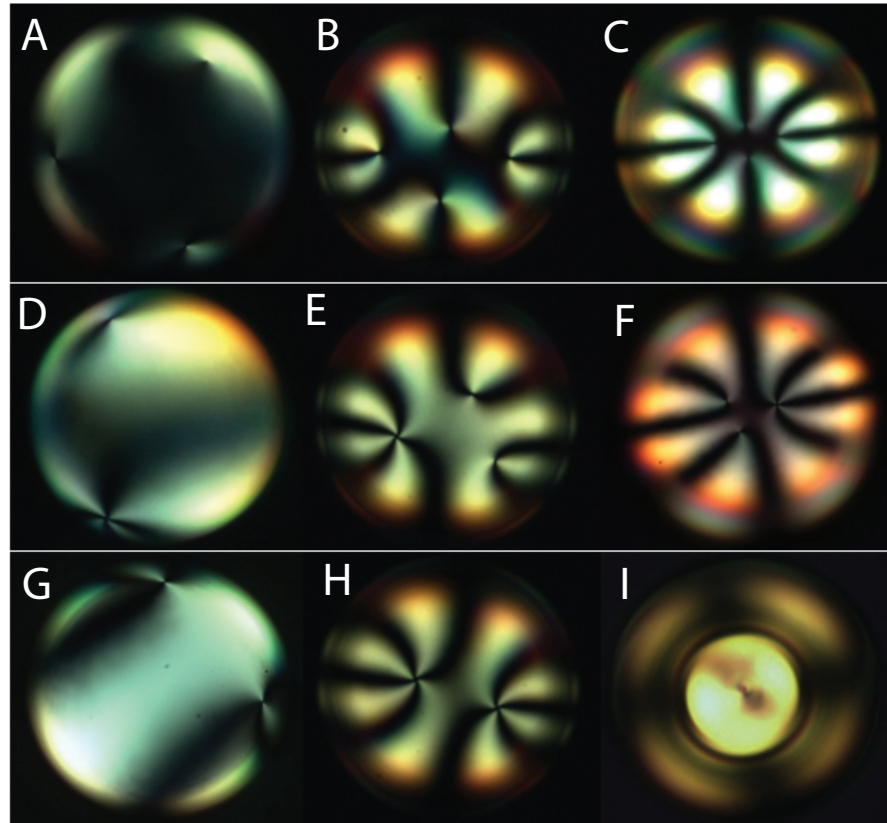
Figure 21: Defect evolution with thickness inhomogeneity. Cross-polarised images illustrating the various angular configurations of the defects in shells with four defects (A-C), shells with three defects (D-F) and shells with two defects (G-I) for different values of the shell thickness. Thickness and thickness inhomogeneity increase from left to right. Ref. [56].

are aligned diametrically (Figs. 11a and 21I). However, upon increasing the thickness inhomogeneity beyond a critical value, one pair migrates rapidly toward the other pair such that eventually all defects are confined to the thinnest section of the shell (Figs. 11b, 11c and 21G-H). This migration is in this chapter called the confinement transition and the reverse process, in which the boojum pairs maximise their angular separation, is referred to as the deconfinement transition. The investigation of these phenomena, and more generally the theoretical study of the director fields and energetics of inhomogeneous divalent nematic shells, is the main concern of this chapter. Although the thickness truly makes this a three-dimensional problem, we are able to use two-dimensional techniques such as conformal mappings to find an *Ansatz* for the

director field in spherical shells. This method is presented in detail in section 3.2. In section 3.3, we study the homogeneous shells as a function of thickness, taking into account the elastic anisotropies. In section 3.4, we construct a phase diagram for inhomogeneous shells that maps out the stability and coexistence of the confined and deconfined configurations as a function of shell thickness and thickness inhomogeneity. Our findings are shown to be in qualitative agreement with recent experimental studies. Finally, the effect of elastic anisotropy on the deconfinement transition is briefly discussed in the concluding section 3.5.

3.2 DIRECTOR FIELDS IN DIVALENT NEMATIC SHELLS

The experimental system under consideration is a nematic double emulsion droplet: a nematic liquid crystal droplet of radius R that encapsulates a smaller water droplet of radius a, as depicted in Fig. 10 and discussed in section . We defined a thickness $h \equiv R - a$ of the shell. Since in general the displacement of the inner water droplet out of the centre of the nematic droplet, Δ, is nonzero, h should be thought of as an average quantity. A surfactant or polymer is added to the inner and outer water phases for two reasons. First of all, it stabilises the double emulsion droplet, because it prevents the inner water droplet to coalesce with the continuous water phase. Secondly, it anchors the nematic molecules parallel to the interfaces. In modelling this experimental system we will employ elasticity theory for nematic liquid crystals, in which one constructs a Frank free energy functional as an expansion in spatial distortions of the local average orientation of the molecules, *i.e.* the unit director field, $\mathbf{n}(\mathbf{x})$, that respect the symmetries of the nematic liquid crystal [18, 40]:

$$
\begin{aligned}
F[\mathbf{n}(\mathbf{x})] = \frac{1}{2} \int dV \left(K_1 \left(\nabla \cdot \mathbf{n} \right)^2 + K_2 \left(\mathbf{n} \cdot \nabla \times \mathbf{n} \right)^2 \right. \\
\left. + K_3 \left(\mathbf{n} \times \nabla \times \mathbf{n} \right)^2 \right) - K_{24} \int \mathbf{dS} \cdot \left(\mathbf{n} \nabla \cdot \mathbf{n} + \mathbf{n} \times \nabla \times \mathbf{n} \right),
\end{aligned} \tag{107}
$$

provided that we assume that these deformations are small on the molecular length scale. Here, K_1, K_2, K_3 and K_{24} are elastic constants measuring the amount of splay, twist, bend and saddle-splay deformations respectively. In most of the work presented, we will work in the one-constant approximation, in which the splay,

twist and bend elastic constants are taken to be equal: $K = K_1 = K_2 = K_3$. Then, eq. (141) reduces to

$$
\begin{aligned}
F[\mathbf{n}\,(\mathbf{x})] = {} & \frac{1}{2} K \int dV \, (\partial_i n_j)^2 \\
& - \left(K_{24} - \frac{1}{2} K\right) \int d\mathbf{S} \cdot (\mathbf{n}\nabla \cdot \mathbf{n} + \mathbf{n} \times \nabla \times \mathbf{n}) .
\end{aligned}
\tag{108}
$$

Furthermore, we discard the surface term in eq. (108), effectively taking $2K_{24} = K$. For a typical droplet size of $50 \, \mu m$ the anchoring energy is much larger than the total elastic energy. Therefore, we can take the preferred tangential alignment of the nematic molecules at the interface as a constraint, thus establishing a boundary condition complementing the free energy. Our approach to minimising the free energy with respect to the director field, will be to find a realistic *Ansatz* given certain locations of the defects. By varying these locations for different shell geometries we obtain the energy landscape as a function of defect positions, thickness and thickness inhomogeneity. The technique we employ to obtain the *Ansatz* is the method of conformal mappings. With the inverse stereographic projection we can find an *Ansatz* for a director field in a homogeneous shell (section 3.2.1). Then, by using an electrostatic analogy we can expand the *Ansatz* to the inhomogeneous case (section 3.2.2). An additional numerical minimisation takes care of the escape of the disclination lines in the third dimension.

3.2.1   *The inverse stereographic projection and the Ansatz for the homogeneous shell*

The *Ansatz* for the director $\mathbf{n}$ of the homogeneous bipolar shell, with two straight disclination lines along the z-axis, simply reads

$$
\mathbf{n}\,(\mathbf{x}) = \cos\alpha \, \hat{\theta} + \sin\alpha \, \hat{\phi},
\tag{109}
$$

where $\hat{\theta}$ and $\hat{\phi}$ are the unit vectors corresponding to the zenith, θ, and azimuthal, ϕ, angles respectively. Note that α is the angle over which $\mathbf{n} = \hat{\theta}$ is rotated at each point on the sphere with respect to an orthonormal reference frame. Thus, the director fieldlines for $\alpha = 0$ and $\alpha = \pi/2$ correspond to the meridians and circles of latitude. To find the *Ansatz* for any other locations of the disclination lines, however, we perform an inverse stereographic projection (Fig. 22). A director field in the flat uv-plane (Fig. 23), minimising
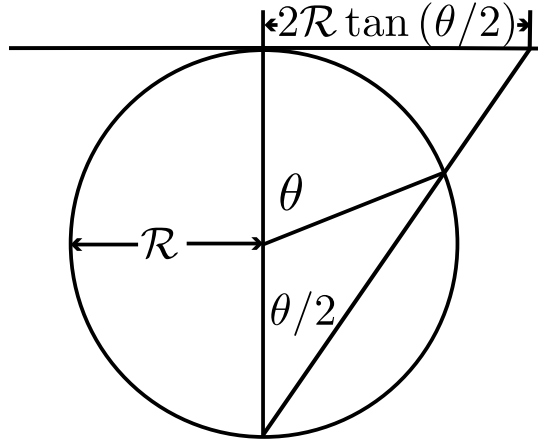
Figure 22: The inverse stereographic mapping given by eq. (248) of the the uv-plane onto the sphere with radius $\mathcal{R}$.

the free energy (see appendix A), is projected onto the concentric surfaces of spheres with radii, $\mathcal{R}$, varying between a and R, *i.e.* $a \leq \mathcal{R} \leq R$, that fill up the shell. Hereby, angles are preserved, *i.e.* this mapping is conformal. This director field contains two charge-one point defects, as we eventually wish to construct an *Ansatz* with two charge-one line defects spanning the shell. We find (see
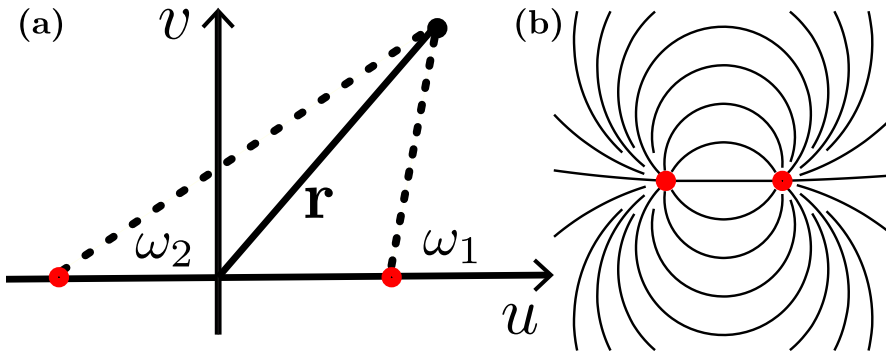

Figure 23: (a) Point defects (red dots) in the uv-plane located at $(u_i, 0)$. The angular director field, $\Phi(\mathbf{r})$ is the sum of the single defect solutions $\Phi_i = \omega_i$. (b) Schematic of the resulting fieldlines.

appendix A)

$$\mathbf{n} = \cos\left(\Phi - \phi\right)\hat{\boldsymbol{\theta}} + \sin\left(\Phi - \phi\right)\hat{\boldsymbol{\phi}}. \tag{110}$$

with Φ given by

$$\Phi = \alpha + \sum_{i=1,2} \arctan\left(\mathcal{Y}_i, \mathcal{X}_i\right), \tag{111}$$

$$\mathcal{X}_i = \tan\left(\frac{\theta}{2}\right)\cos\phi - \operatorname{sgn}\left(u_i\right)\tan\left(\frac{\theta_i}{2}\right), \tag{112}$$

$$\mathcal{Y}_i = \tan\left(\frac{\theta}{2}\right)\sin\phi, \tag{113}$$

as the director field on the sphere, depicted in Fig. 24. In ref. [57] it was shown that this field on the sphere minimises the free energy in the one-constant approximation, provided that it possesses two charge-one defects. They are located at zenith angles

$$\theta_i = 2\arctan\left(\frac{|u_i|}{2\mathcal{R}}\right). \tag{114}$$

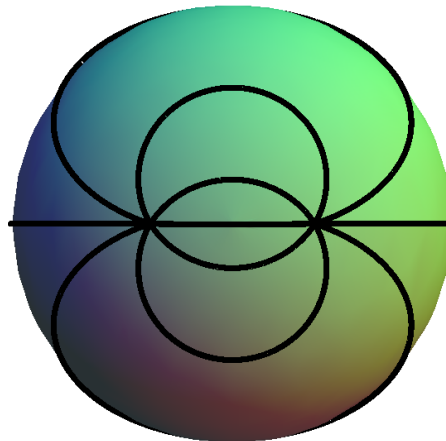At the same time this expression is an *Ansatz* for a homoge-

Figure 24: Top view of the director field on the sphere, given by eq. (110).

neous shell with two straight disclination lines spanning the shell, provided we build it out of concentric spheres of radius $\mathcal{R}$. The director lies along the spheres, including the special case that these spheres are the surfaces of the inner or outer droplets. Therefore, the tangential boundary conditions are satisfied.

3.2.2   *An electrostatic analogy and the Ansatz for the inhomogeneous shell*

The concentric spheres that fill up the homogeneous shell are displaced if the shell is inhomogeneous. Moreover, the disclination

lines are no longer straight. To construct an *Ansatz* for the director in inhomogeneous shells we need to find equations for the displaced spheres and the defect lines. For this, we exploit an electrostatic analogy, namely, calculating the equipotential (solid in Fig. 25) and electric (dashed green) field lines of an infinitely long charged line running parallel to a conducting plane (blue) at a distance d. By the method of images, solving this electrostatic
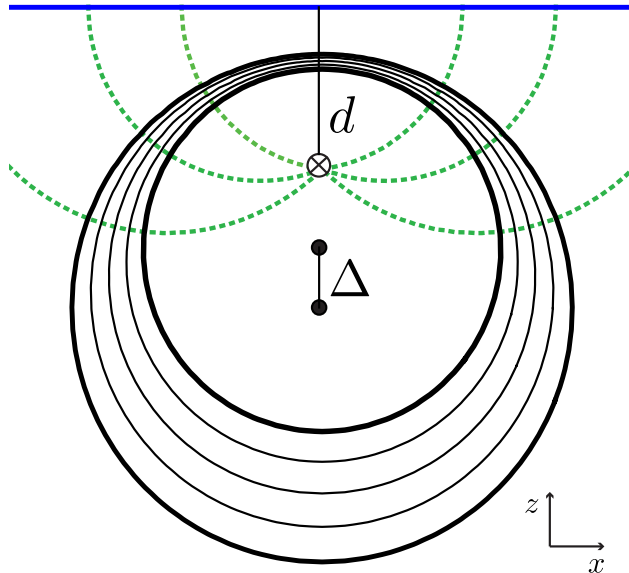
Figure 25: Equipotential (solid) and field (dashed green) lines of an infinitely long charged line, indicated with a cross, running along the y-direction, parallel to a conducting plane (blue) at a distance d. The two equipotential circles, drawn in bold, correspond to two non-concentric droplets whose centres, indicated by dots, are displaced by Δ.

problem is equivalent to solving for the equipotential and electric field lines of two oppositely charged parallel running cylinders, or, equivalently, a 2D point charge and its mirror charge. These can be extracted from the complex potential [91, 30]

$$\psi\left(w\right) = \log\left(\frac{w + id}{w - id}\right). \tag{115}$$

where $w = x + iz$ is a complex number. Note that ψ is a conformal transformation, just like the inverse stereographic projection is, mapping a region bounded by two non-concentric circles into a vertical strip (see appendix B). Thus, the level curves of the real and imaginary parts of $\psi\left(w\right)$ are the equipotential and electric field lines, respectively. These two families of orthogonal lines,

together forming what is known as an isothermic net, read mathematically

$$\Re[\psi(w)] = \log\left|\frac{w+id}{w-id}\right| = \text{constant},\tag{116}$$

$$\Im[\psi(w)] = \arg\left(\frac{w+id}{w-id}\right) = \text{constant}.\tag{117}$$

We see that eq. (116) describes circles of Apollonius (see appendix B) with inverse points $\pm id$. We can rewrite it as

$$x^2 + (z-\eta)^2 = \mathcal{R}^2,\tag{118}$$

with radius, $\mathcal{R}$, and displacement with respect to the origin, η, which are related by

$$\mathcal{R}^2 = \eta^2 - d^2.\tag{119}$$

Rotating the circular equipotential lines around the z-axis creates the non-intersecting spheres. By choosing two of these spheres (drawn in bold in Fig. 25) as the surfaces of our inner and outer droplets in addition to a choice of d, we can fix the geometry. The relative displacement of the inner droplet with respect to its concentric position, Δ, is given by

$$\Delta = \eta_a - \eta_R,\tag{120}$$

where η_a and η_R are the vertical displacements from the origin of the inner and outer spheres, respectively. We take $\eta < 0$, such that $\Delta > 0$. This implies that the thinnest part of the shell is at the top, like in Figs. 25 and 10. The other spheres fill up the shell. Since the spheres are the surfaces of revolution of the circles around the z-axis, we obtain the equation for the spheres simply by addition of y^2 to the left hand side of eq. (118):

$$x^2 + y^2 + (z-\eta)^2 = \mathcal{R}^2.\tag{121}$$

Two independently chosen electric field lines will serve as disclination lines. These lines run perpendicular to the equipotential lines, and thus perpendicular to the surface of the inner and outer droplet, as is demanded by the tangential boundary conditions. Similar to the calculation of the equipotential lines, one can obtain the equations for the electric field lines from eq. (117) (appendix B). We find that the electric field lines are also circles:

$$(x-\epsilon)^2 + z^2 = S^2,\tag{122}$$

with radii, S, and displacements, ϵ, now in the x-direction, which are related as follows:

$$S^2 = \epsilon^2 + d^2. \tag{123}$$

Since only the circular arc that is inside the shell matters, we care about the points of intersection of the two defect lines with the spheres that fill up the shell. We would like to find the zenith angle on each sphere, β_i , that these points of intersection make. We assign a different character than θ_i, because β_i does not have a constant value as it depends on the displacement (or radius) of the sphere. Let us therefore refine our definition of θ_i as the zenith angle of the defect on the outer-most sphere. Now, the following geometrical relations hold:

$$x = \pm\mathcal{R}\sin\beta_i, \tag{124}$$

$$z = \eta + \mathcal{R}\cos\beta_i. \tag{125}$$

Then, by substituting x and z in eq. (122) and eliminating d in favour of $\mathcal{R}$ by applying eq. (119) we find an expression for ϵ_i as a function of β_i, η and $\mathcal{R}$ (assuming $\sin\beta_i \neq 0$):

$$\epsilon_i = \pm\frac{\mathcal{R} + \eta\cos\beta_i}{\sin\beta_i} = \pm\frac{\mathcal{R} + \eta_{\mathcal{R}}\cos\theta_i}{\sin\theta_i} \tag{126}$$

where the last equality follows from the constantness of ϵ_i, as we are moving along the same circle. We find the solution for β_i

$$\beta_i = 2\arctan\left(\frac{\epsilon_i + \sqrt{\epsilon_i^2 + d^2}}{\mathcal{R} - \eta}\right). \tag{127}$$

Not surprisingly, β_i is increasing as the radius of the sphere is decreasing. If $\theta_i = 0$ or $\theta_i = \pi$, the disclination lines are straight and $\beta_i = 0$ or $\beta_i = \pi$, respectively. Next, we find η as a function of the spatial coordinates x, y and z, since it is the only variable, besides the parametric dependence on d and θ_i, on which β_i is depending. Put differently, given some point in space, on which sphere is it? To answer this question we resort to eq. (121), yielding the following result:

$$\eta\left(\mathbf{x}\right) = \frac{x^2 + y^2 + z^2 + d^2}{2z}. \tag{128}$$

We have now acquired all the necessary information to construct the *Ansatz* for the director field in an inhomogeneous shell. We

take the *Ansatz* for the director field in a homogeneous shell, eq. (110), and make the following replacements

$$\theta_i \to \beta_i, \tag{129}$$

$$z \to z - \eta. \tag{130}$$

The first substitution concerns the defect lines. The second accounts for the displacement of the spheres and implies the substitution

$$\theta \to \beta = \arccos\left(\frac{(z-\eta)}{x^2 + y^2 + (z-\eta)^2}\right), \tag{131}$$

with β being the zenith angle on the displaced sphere. Finally, together with eqs. (126)-(131) we obtain the *Ansatz* for the director in inhomogeneous shells with two charge-one disclination lines:

$$\mathbf{n} = \cos\left(\Phi - \phi\right)\hat{\boldsymbol{\beta}} + \sin\left(\Phi - \phi\right)\hat{\boldsymbol{\phi}}. \tag{132}$$

where Φ is now given by

$$\Phi = \alpha + \sum_{i=1,2} \arctan\left(\mathcal{Y}_i, \mathcal{X}_i\right), \tag{133}$$

$$\mathcal{X}_i = \tan\left(\frac{\beta}{2}\right)\cos\phi - \operatorname{sgn}\left(u_i\right)\tan\left(\frac{\beta_i}{2}\right), \tag{134}$$

$$\mathcal{Y}_i = \tan\left(\frac{\beta}{2}\right)\sin\phi. \tag{135}$$

The disclination lines can be put anywhere except for the south pole. In the case of a bipolar defect arrangement, i.e. $\theta_i = 0$ and $\theta_i = \pi$, we draw on each sphere the director given by eq. (109), with the substitution in eq. (131) and find an *Ansatz* for the bipolar inhomogeneous shell that reads

$$\mathbf{n}\left(\mathbf{x}\right) = \hat{\boldsymbol{\beta}} = \cos\beta\cos\phi\hat{\mathbf{x}} + \cos\beta\sin\phi\hat{\mathbf{y}} - \sin\beta\hat{\mathbf{z}}. \tag{136}$$

The *Ansatz* is then subjected to a numerical minimisation, employing the finite element method [93] suitable for non-trivial geometries, to ensure the escape of the disclination lines leaving a point defect at the inner and outer surface for each line (see Figs. 26a and 26b). We refine the mesh at these defects to obtain good accuracy on the rapidly changing director (Fig. 26c).
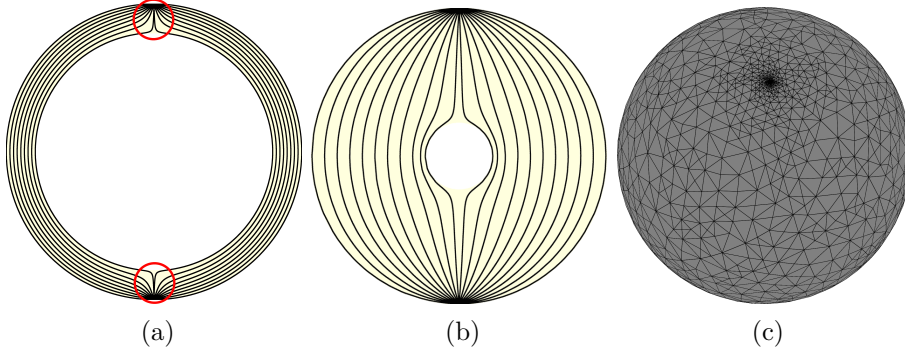
Figure 26: (a,b) Director field of the shell for (a) $\frac{h}{R} = 0.2$ and (b) $\frac{h}{R} = 0.77$. The disclination lines escape in the third dimension leaving two pairs of boojums. Each pair is encircled in red in (a). The director field in (b) resembles a slightly distorted director field of a single nematic droplet. (c) A typical mesh used in the numerical minimisation is refined around the locations of the defects.

3.3 ENERGETICS OF HOMOGENEOUS SHELLS

First, we calculate the free energy for the *Ansatz* in (109), in which the defects are located at opposite poles on the sphere, by integrating the free energy density over the spherical shell except for a cut-off region determined by $0 < \theta < \frac{b}{r}$ and $\pi - \frac{b}{r} < \theta < \pi$ with r the radial coordinate. The result reads

$$
\begin{aligned}
F =& 2\pi \left(K_1 \cos^2 \alpha + K_3 \sin^2 \alpha \right) \\
& \left(R \log \frac{2R}{b} - (R - h) \log \frac{2(R - h)}{b} - 2h \right) \\
& + 2\pi \left(K_3 - 2K_{24} \right) h \quad\quad\quad\quad\quad (137) \\
\xrightarrow{K_i = K} & 2\pi K \left(R \log \frac{2R}{b} - (R - h) \log \frac{2(R - h)}{b} - 2h \right).
\end{aligned}
$$

$$(138)$$

Note that splay and bend deformations can be transformed into each other by tuning α, but the total energy is unchanged if $K_1 = K_3$, as is shown graphically in Fig. 27a. Furthermore, note that the saddle-splay term is proportional to the thickness, in contrast to the splay and bend energy which both contain a logarithmic divergence. We therefore expect that, as a first approach, it is not so important in determining the defect locations. Since these defects repel each other, for homogeneous shells we always find
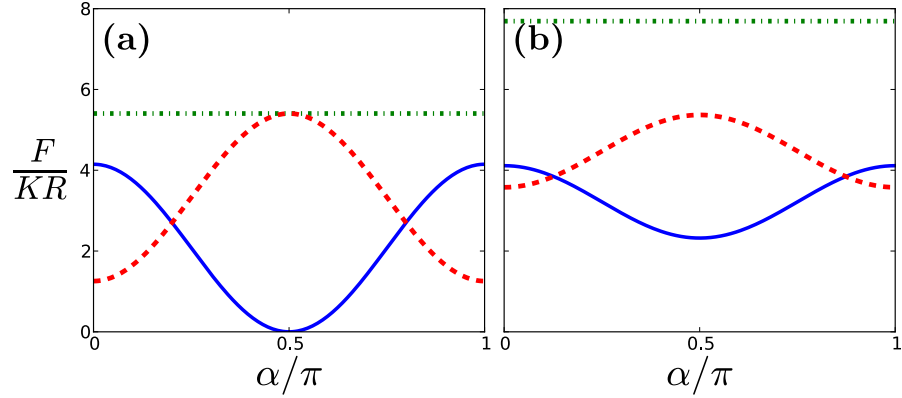
Figure 27: The splay (solid blue), bend (dashed red), and their sum
(dashed-dotted green) as a function of α when (a) $\theta_{12} = \pi$
and (b) $\theta_{12} = 0.1\pi$, in both cases $\frac{b}{R} = 0.025$.

this bipolar arrangement as the free energy minimum, irrespective
of thickness. Placing the defects at a different angular separation,
θ_{12}, from each other, eq. (110), leads to an increase in the elastic
energy, since $F \sim -\log\left(1 - \cos\theta_{12}\right)$ [57, 70, 105]. Moreover, the
splay and bend cannot be efficiently transferred into one another
by a global rotation (changing α), e.g. splay no longer vanishes for
$\alpha = \pi/2$ whereas it did for eq. (109). This is presented graphically
in Fig. 27b. Note that the director field minimising the free energy
for $K_1 \neq K_3$ is not equal to the *Ansatz* [3, 88, 23, 55, 49]. Besides
the elastic anisotropy the escape of the defect lines in the third
dimension modifies the energetics. As a result, there are two pairs
of boojums residing on the interfaces. We can effectively take the
escape into account in our calculations of the energy by replacing
the cut-off b by the thickness h and adding $4.2\pi K h$ for each pair
of boojums[105, 11]. We obtain in the one-constant approximation

$$F = 2\pi K \left(R \log \frac{2R}{h} - (R - h) \log \frac{2\left(R - h\right)}{h} + 2.2h \right). \quad (139)$$

In Fig. 28 we compare this analytical estimate with numerical re-
sults from our procedure outlined in the previous section. We find
a good agreement, in particular for small $\frac{h}{R}$, as expected. In this
regime, the free energy rises as the volume of the shell increases.
For large $\frac{h}{R}$, our result deviates from eq. (139). Remarkably, as the
thickness is increased, the free energy decreases after some critical
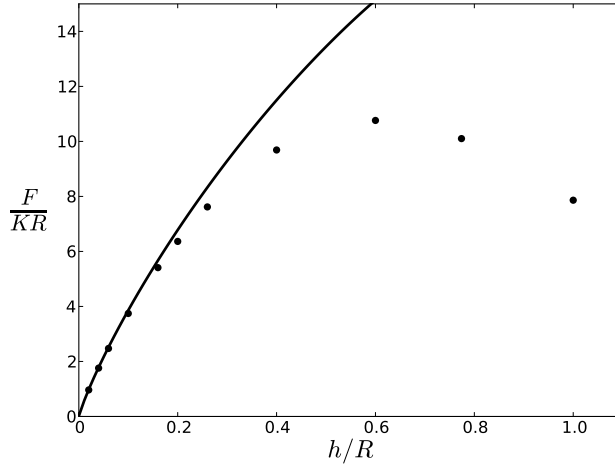value, $h^*/R \approx 0.6$. The size of the inner droplet, which is $2a$, is no

Figure 28: Free energy of the bipolar shell as a function of thickness. The line is given by the analytical estimate in eq. (139).

longer larger that the scale over which the escape happens, which is roughly h. Equating these two length scales gives a consistent back-of-the-envelope estimate $h^*/R \approx 2/3$. As a result, when h becomes comparable to R, the inner droplet no longer forms an obstruction that makes the shell locally look like a slab in which the lines can escape. Rather, the point of view that a slight director distortion is induced in a single nematic droplet (resulting in an energy cost) is more appropriate in this regime. This cross-over is illustrated in Figs. 26a and 26b.

3.4 ENERGETICS OF INHOMOGENEOUS SHELLS

3.4.1 *Buoyancy versus elastic forces*

Before we study the effect of the thickness inhomogeneity on the mechanics of the nematic liquid crystal, we first investigate its origin. In our experiments we observe that the inner water droplet is displaced along the vertical direction. This implies that gravity plays its part, but it does not necessarily mean that it is the density mismatch between the nematic and water that drives the motion of the inner droplet. Another possibility would be that the elastic forces push the droplet out of the centre, while gravity only breaks the symmetry. To identify the origin of the thickness inhomogeneity, we will compare the magnitude of the elastic forces

with Archimedes force. Therefore we map out the elastic energy as a function of the displacement $\frac{\Delta}{h}$ for several values of $\frac{h}{R}$, as shown in Fig. 29. Our first observation is that the stability of this pertur-
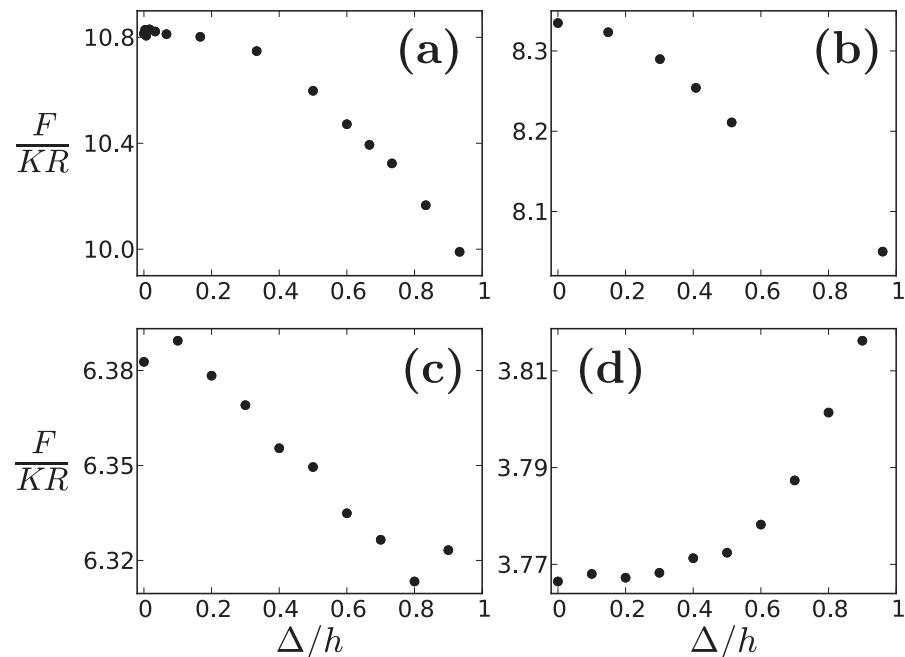

Figure 29: The elastic free energy of the liquid crystal as a function of the relative displacement of the inner droplet. In (a), (b) and (c), $\frac{h}{R} = 0.6, 0.3, 0.2$, respectively, the energy is minimised when the droplet is on the periphery of the larger droplet, resulting in an elastic force of the order of K pushing the inner droplet outwards. (d) For a thinner shell with $\frac{h}{R} = 0.1$, there is a restoring force on the inner droplet, driving it back to the centre of the outer one.

bation is a nontrivial function of the thickness. For $\frac{h}{R} = 0.2, 0.3, 0.6$ we observe that the energy decreases as a function of Δ. This is in agreement with a calculation done for $\frac{h}{R} = 0.77$ in ref. [24]. However, for a relative thin shell of $\frac{h}{R} = 0.1$ there is an elastic minimum for $\Delta = 0$. Second, the magnitude of the elastic force is less than or of the order of $f_e \sim K \approx 10^{-11} N$. This is much smaller than the net force from buoyancy and the weight of the droplet $f_b = (\rho_{nem} - \rho_w) gV$ with the volume of the water droplet $V = \frac{4}{3}\pi a^3$. For $a \approx 50 \, \mu m$ and a difference in density between 5CB and water of roughly $3 \times 10 \, kg \, m^{-3}$ at room temperature[19], we find $f_b \approx 2 \times 10^{-10} N$. Therefore, we conclude that buoyancy is

indeed responsible for displacing the inner water droplet from the centre in our experiments. If one would try to match the density of the nematic to the water density, as was done in some of the experiments in ref. [24], where the density difference was brought down to $2 \ kg \ m^{-3}$, f_b and f_e will be of the same order, but only when the inner droplet is at the periphery. Also in the regime of small a these forces will become comparable.

3.4.2 *Confined and deconfined defect configurations*

In the remainder of this chapter we will compare two distinct defect configurations. In one configuration the defects are at maximum angular separation from each other at opposite sites on the sphere. We will refer to this as the deconfined state. In the other case the defects are trapped or confined to the thinnest top part of the shell. The defects are located symmetrically at an angle θ_i from the vertical axis so that their angular separation is simply $\theta_{12} = 2\theta_i$ (provided that $2\theta_i \leq \pi$). The energy can be estimated to grow with the thickness of the shell where the defects are located. This is roughly the minimal thickness at the top of the shell, for which there is a simple geometrical relation $h_{min} = h - \Delta$. From this one immediately sees that h and Δ take opposite roles. We thus expect the confined state to be energetically favourable over the deconfined state when the shell is sufficiently thin and inhomogeneous, *i.e.* low h and high Δ. This heuristic argument has led us to a systematic study of the energy landscape as a function of defect location. We classify three cases: I) the confined state is the only energy minimum, see Figs. 30a and 31a; II) both the confined and deconfined state are minima, one of them is local and the other is global, see Fig. 30b; III) the deconfined state is the only energy minimum, see Fig. 30c and 31b-c.

3.4.3 *Phase diagram*

We construct a phase diagram as a function of thickness and thickness inhomogeneity. We find that for a given thickness there is a deconfined minimum below a critical value of the relative displacement $\frac{\Delta_c}{h}$, marked green in Fig. 32, which is monotonously increasing with the thickness. The confined state is found to min-
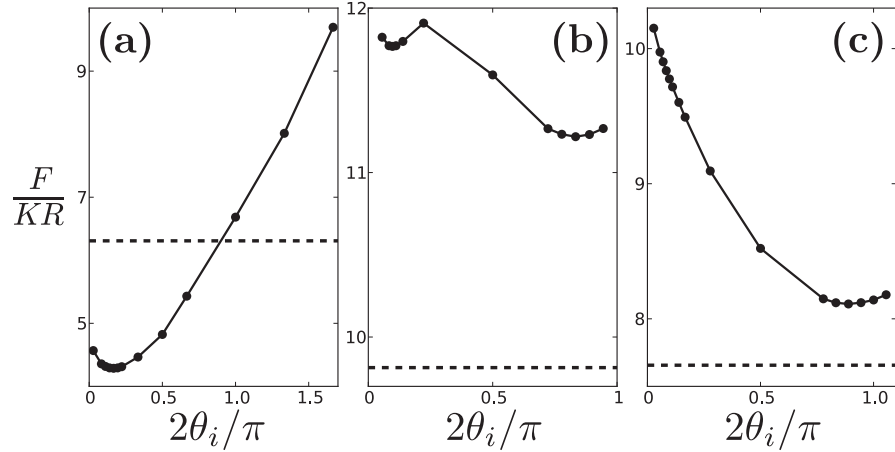
Figure 30: The free energy for a shell as a function of the central angle between two defects on the outer surface in the confined configuration, when (a) $\frac{h}{R} = 0.2$ and $\frac{\Delta}{h} = 0.831$, (b) $\frac{h}{R} = 0.7$ and $\frac{\Delta}{h} = 0.939$, (c) $\frac{h}{R} = 0.8$ and $\frac{\Delta}{h} = 0.946$. Note that for $2\theta_i = \pi$ the defects are aligned horizontally, rather than vertically as in the deconfined conformation. The dashed line indicates the energy of the deconfined configuration. These graphs suggest a confined global minimum at $\frac{\theta}{\pi} \approx 0.17$ in (a), a local confined minimum at $\frac{\theta}{\pi} \approx 0.1$ and a global deconfined minimum in (b) and a global deconfined minimum in (c).

imise the energy (at least) locally above another critical value, $\frac{\Delta_d}{h}$, marked in purple in Fig. 32, which is also larger for thicker shells. Therefore, as anticipated in the previous section, we find that the confined defect state minimises the elastic energy for thin and inhomogeneous shells, whereas the deconfined defect state minimises the energy for rather homogeneous and thick shells. Since these two critical values for $\frac{\Delta}{h}$ are different there exist two minima for $\frac{\Delta_d}{h} < \frac{\Delta}{h} < \frac{\Delta_c}{h}$. We can thus divide the phase diagram into three regions: a deconfined minimum-only, confined minimum-only and coexisting region coloured purple, green and blue in Fig. 32, respectively. These phases are separated by lines marking where, as in a first-order phase transition, a local energy minimum is lost. We remark that the energy differences between the deconfined and weakly confined states for thin and homogeneous shells become too small to conclude with certainty that $\frac{\Delta_c}{h}$ goes to a finite value and the deconfinement transition reaches $\frac{\Delta_d}{h} = 0$ at extremely low h.
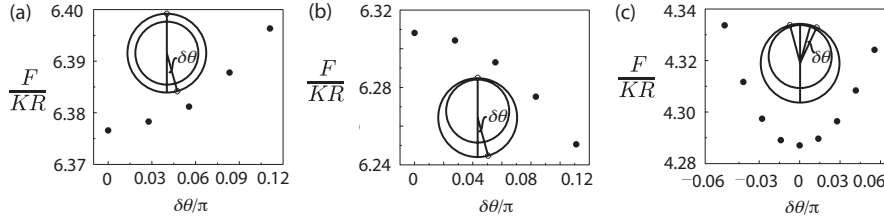
Figure 31: (a) Free energy of a shell of uniform thickness with $h/R = 0.2$, as a function of the angular perturbation of one of the two pairs of defects, $\delta\theta$. When $\Delta = 0$ the inner and outer drops are concentric and $\theta_{12} = \pi$ minimises the free energy irrespective of thickness. (b) Free energy of a shell with $\Delta/h = 0.831$, as a function of $\delta\theta$. In this case, the $\theta_{12} = \pi$ arrangement no longer minimizes the free energy. (e) Free energy as a function of the angular perturbation from the elastic-energy minimum, which is located at $30°$ for the shell in (b).

3.4.4 *Comparison with experiment*

In this section we make a comparison with the experiments on nematic double emulsion droplet performed in the lab of Alberto Fernandez-Nieves. The nematic double emulsion droplets create inhomogeneous shells, because buoyancy displaces the inner droplet upward from its concentric position along the gravitational direction. The short-range steric repulsion from the polymer polyvinyl alcohol (PVA), prevents the inner droplet from coalescing with the continuous phase [56, 41]. Therefore, we assume that the thinnest part of the shell, h_{min}, is effectively constant. By osmosis the thickness inhomogeneity can be modified. We find

$$\frac{\Delta}{h} = 1 - \frac{u_0}{u} \sqrt[3]{\frac{1 - (1 - u)^3}{1 - (1 - u_0)^3}} \tag{140}$$

where $u \equiv \frac{h}{R}$ and u_0 is the value of u when the shell becomes homogeneous, see appendix C. This path through the phase diagram is indicated in red in Fig. 32. If we traverse this path in the direction of decreasing thickness we find that the angular separation between the defects, θ_{12}, changes abruptly from π to a value much smaller than that, as does the order parameter in a first-order phase transition. In the model this occurs in both theory (red squares in Fig. 33) at $u/u_0 \approx 30$ and in the experiment
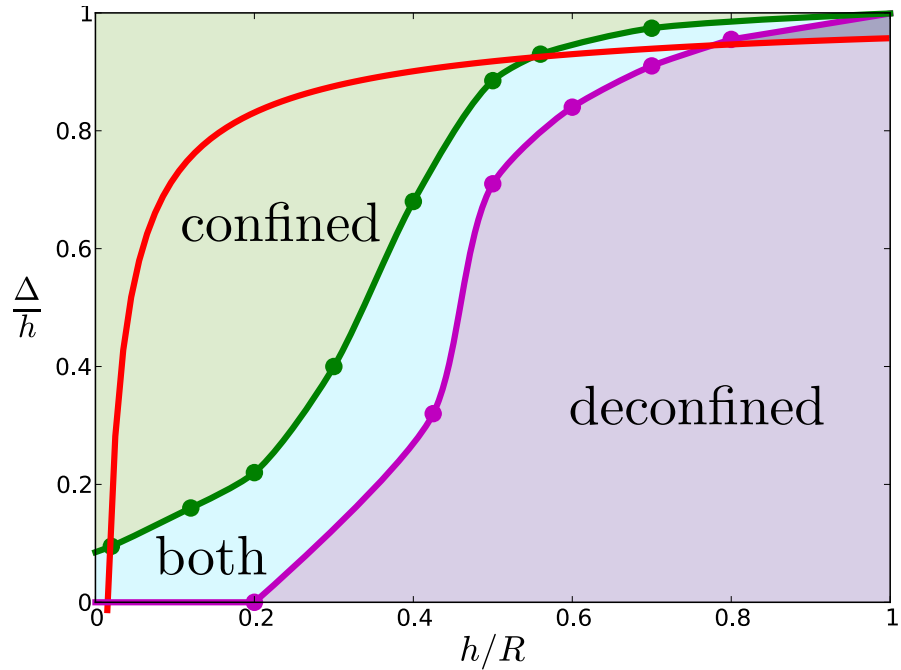
Figure 32: Phase diagram of the confined (green), deconfined (purple) and coexistence phase (blue) as a function of thickness of the shell, $\frac{h}{R}$, and thickness inhomogeneity, $\frac{\Delta}{h}$. The confinement (green), $\frac{\Delta_c}{h}$, and deconfinement (purple), $\frac{\Delta_d}{h}$, transition lines separate these phases. The red line represents the assumed experimental trajectory of constant h_{min}.

(black circles in Fig. 33) at $u/u_0 \approx 20$. The abruptness of the confinement transition is marked by the the short timescale of only tens of seconds, compared to the hours over which the osmosis occurs, in which the pair of defects located at the thicker hemisphere moves toward the top of the shell (see Fig. 34). Upon decreasing the thickness and consequently the thickness inhomogeneity even further the defects spread and the angular separation increases again. When the shell is approximately homogeneous (Fig. 35a), the effect of confinement has weakened so much that the defects are aligned antipodally. The axis joining them can now point in any direction though, as shown by the two shells in Figs. 35b and 35c. In this case, the energy of the thin shell does not depend on the orientation of this axis, in contrast to what happens for thicker shells, whose boojums axis are aligned along the gravitational direction. This also confirms that the defect deconfinement transition in the phase diagram goes to $\Delta = 0$ for low h. Upon
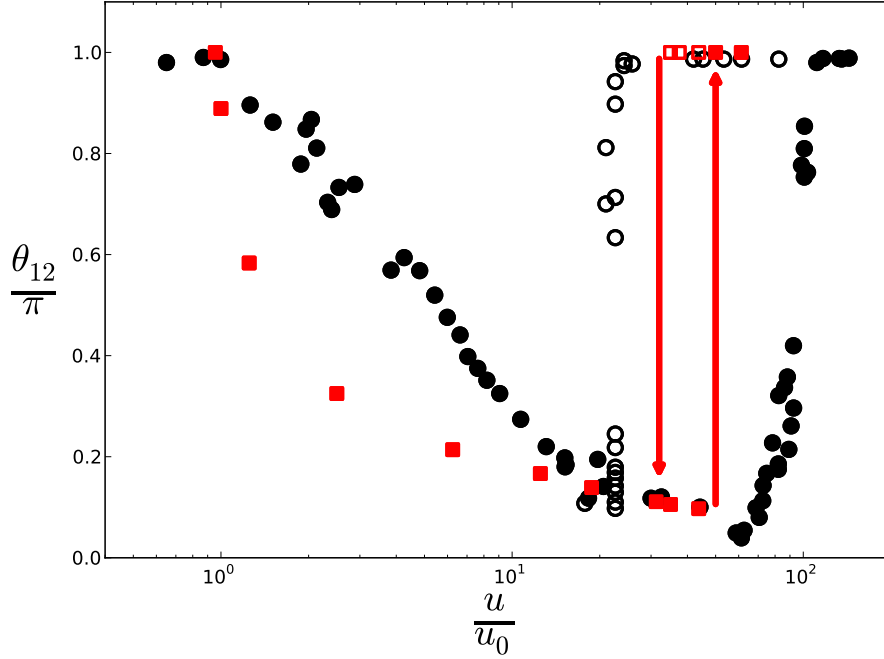
Figure 33: Angular separation between the defects as a function of nor-
malised shell thickness, u/u_0, in the experiment (black cir-
cles) [41] and in theory (red squares). An increase (decrease)
of u/u_0 is established by shrinking (expanding) the inner
water droplet. The open symbols depict the hysteresis.

reversing the path through the phase diagram, *i.e.* traverse the red
path in Fig. 32 in the direction of increasing thickness, we first find
that the defects move toward each other gradually. Upon increas-
ing the thickness even further we find that θ_{12} increases rapidly
to its maximum possible value at $\frac{u}{u_0} \approx 50$ and $\frac{u}{u_0} \approx 80$ in the
model and experiment, respectively, as the mutual repulsion be-
tween the pairs of defects becomes too large. It is thus favourable
to have one pair of boojums at the thickest part of the shell. Note
that the thickness at which this deconfinement transition occurs
is thus larger than the thickness at which the confinement transi-
tion occurs. This hysteresis between the confinement and decon-
finement transitions is due to phase coexistence. The green and
purple curves in Fig. 32 (corresponding to the confinement and
deconfinement transition) intersect the red curve (assumed experi-
mental path) at different points in the phase diagram. Finally, we
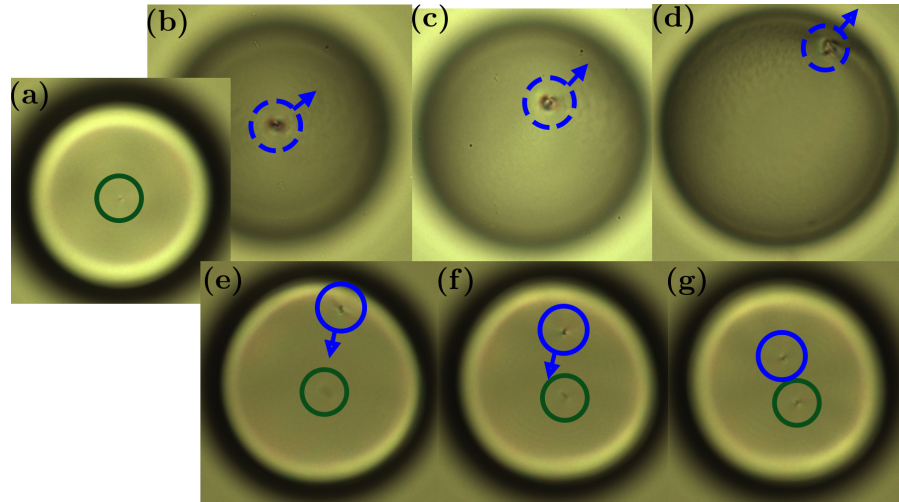remark that we have not observed any splitting of the defects into

Figure 34: Bright field images of a shell (top view) undergoing the confinement transition. (a) One defect pair, encircled in green, is at the top of the shell before the transition. The other pair of boojums, encircled in blue, moves from the lower hemisphere in (b)-(d) to the upper hemisphere in (e)-(g).The arrow indicates the direction of motion. The circle is dashed if the defect pair is located in the lower hemisphere. The time span is tens of seconds. $2R = 133 \ \mu m$ and $2a = 125 \ \mu m$. Ref. [41].

disclination lines of charge one-half during this process of shell thinning and thickening.

3.5 CONCLUSION

In this study, we have crossed from a two-dimensional description of a spherical nematic liquid crystal to a spherical divalent shell with a finite thickness and possible inhomogeneity. Irrespective of thickness, we always find an antipodal arrangement as the free energy minimum in homogeneous shells of nematic liquid crystals. However, this scenario changes when the shell thickness is sufficiently inhomogeneous. The repulsion between the pairs of boojums competes with the minimisation of the distance between the defects within a pair. As a result, the defects undergo a confinement transition to the thinnest part of the shell. Conversely, the defects confined in the thinner hemisphere make a deconfinement transition that maximises their separation. The critical displace-

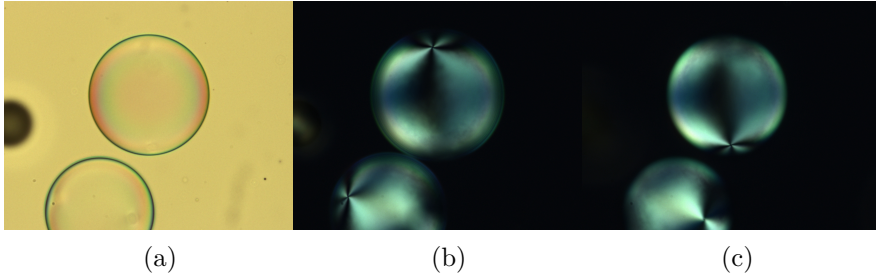(a)   (b)   (c)

Figure 35: (a) Bright field image of two thin shells obtained after osmotically shrinking the corresponding thicker shells. The location of the defects are easily seen in cross-polarisation by (b) focusing the shells at the top, to see the upper pair of boojums, and (c) at the bottom, to see the lower pair of boojums. The defects are a diameter away, with $\theta_{12} = \pi$. Interestingly, for these thin shells, the direction of the axis joining the two pairs of boojums is not correlated with the gravitational z-axis. The dimensions of the upper shell are $2R = 138.8\ \mu m$ and $2a = 137.5\ \mu m$, corresponding to $u/u_0 = 1.05$. Ref. [41].

ment of the inner droplet for which these transitions occur are in general not equal, i.e. there is hysteresis present. These transitions are also present in our experiment, where a water droplet encapsulates a nematic liquid crystal droplet to make a spherical nematic shell. We have showed that these shells are inhomogeneous due to the buoyancy that displaces the inner droplet along the gravitational direction. Additional to the confinement and deconfinement transitions, a continuous evolution is observed, when thin shells become less inhomogeneous. Though we found an excellent qualitative agreement between theory and experiment for all these phenomena, an exact quantitative agreement is still lacking, possibly due to a lack of validity of the one-constant approximation. It would be interesting to extend this study by investigating the role of elastic anisotropy on the defect transitions in nematic shells. Since it is more difficult to exchange splay and bend when the defects are confined, there will be more distortions of the type weighted with the largest Frank constant in this state and we expect that the region in the phase diagram occupied by the confined state will be smaller if elastic anisotropy is included. This would imply that the confinement and deconfinement transitions occur

at smaller thickness if $K_1 \neq K_3$. It should be noted though that the *Ansatz* will no longer be accurate if the elastic anisotropy is large. Finally, it would be worthwhile to pursue a study on chirality in nematic shells, because chirality can emerge spontaneously in geometrically confined liquid crystals (see chapter 4).